1 **Abrupt excursion in water vapor isotopic variability during cold fronts at**

2 **the Pointe Benedicte observatory in Amsterdam Island**

3

4 Amaëlle Landais[1,*], Cécile Agosta[1,*], Françoise Vimeux[1,2], Olivier Magand[3], Cyrielle Solis[1],

5 Alexandre Cauquoin[4], Niels Dutrievoz[1], Camille Risi[5], Christophe Leroy-Dos Santos[1], Elise

6 Fourré[1], Olivier Cattani[1], Olivier Jossoud[1], Bénédicte Minster[1], Frédéric Prié[1], Mathieu

7 Casado[1], Aurélien Dommergue[6], Yann Bertrand[6], Martin Werner[7]

8

9 [1] Laboratoire des Sciences du Climat et de l'Environnement, LSCE/IPSL, CEA-CNRS-UVSQ,
10 Université Paris-Saclay, 91191 Gif-sur-Yvette, France
11
12 [2] HydroSciences Montpellier (HSM), UMR 5569 (UM, CNRS, IRD), 34095 Montpellier, France
13
14 [3] Observatoire des Sciences de l'Univers à La Réunion (OSU-R), UAR 3365, CNRS, Université de La
15 Réunion, Météo France, 97744 Saint-Denis, La Réunion, France
16
17 [4] Institute of Industrial Science (IIS), The University of Tokyo, Kashiwa, Japan.
18
19 [5] Laboratoire de Météorologie Dynamique, Institut Pierre - Simon Laplace, Sorbonne Université /
20 CNRS / École Polytechnique – IPP, Paris, France
21
22 [6] Univ. Grenoble Alpes, CNRS, INRAE, IRD, Grenoble INP[T], IGE, 38000 Grenoble, France
23 ([T]Institute of Engineering and Management Univ. Grenoble Alpes)
24
25 [7] Alfred Wegener Institute, Helmholtz Centre for Marine and Polar Research, D-27570 Bremerhaven,
26 Germany
27
28 * corresponding authors who contributed equally to the study: amaelle.landais@lsce.ipsl.fr and
29 cecile.agosta@lsce.ipsl.fr
30

31 **Abstract**

32 In order to complement the picture of the atmospheric water cycle in the Southern Ocean, we

33 have continuously monitored water vapor isotopes since January 2020 in Amsterdam Island

34 (37.7983 °S, 77.5378 °E) in the Indian Ocean. We present here the first 2-year-long water

35 vapor isotopic record monitored on this site. We show that the vapor isotopic composition

36 largely follows the vapor mixing ratio, as expected in marine boundary layers. However, we

37 evidence 11 cold front periods of a few days where there is a strong loss of correlation

38 between water vapor $\delta^{18}O$ and mixing ratio. These periods are associated with abrupt negative

39 excursions of water vapor $\delta^{18}O$, often occurring toward the end of precipitation events. Six of

40 these events show a decrease in gaseous elemental mercury suggesting subsidence of air from

41 higher altitude.

42 Accurately representing the water isotopic signal during these cold fronts is a real challenge

43 for the atmospheric components of Earth System models equipped with water isotopes. While

44 the ECHAM6-wiso model was able to reproduce most of the sharp negative water vapor $\delta^{18}O$

45 excursions, the LMDZ-iso model at 2° (3°) resolution was only able to reproduce 7 (1) of the

46 negative excursions. Based on a detail model-data comparison, we conclude that the most

47 plausible explanations for such isotopic excursions are rain-vapor interactions associated with

48 subsidence at the rear of a precipitation event.

49

50 **1. Introduction**

51 The main sources of uncertainty in the atmospheric components of Earth System Models for

52 future climate projections are associated with complex atmospheric processes, particularly

53 those related to water vapor and clouds (Sherwood et al., 2014; Arias et al., 2021). Decreasing

54 these uncertainties is of vital interest as the hydrological cycle is a fundamental element of the

55 climate system because it allows, via the transport of water vapor, to ensure the Earth's thermal

56 balance.

57 Stable water isotopes are a useful tool to study the influence of dynamical processes on the

58 water budget at various spatial and temporal scales. They provide a framework for analyzing

59 moist processes over a range of time scales from large-scale moisture transport to cloud

60 formation, precipitation, and small-scale turbulent mixing (Galewsky et al., 2016; Thurnherr et

61 al., 2020; Bailey et al., 2023; Dahinden et al., 2021).

62 The relative abundance of heavy and light isotopes in different water reservoirs is altered during

63 phase change processes due to isotopic fractionation (caused by a difference in saturation vapor

64 pressure and molecular diffusivity in the air and the ice). Each time a phase change occurs, the

65 relative abundance of water vapor isotopes is altered. We express the abundance of the heavy

66 isotopes D and ^{18}O with respect to the amount of light isotopes ^{16}O and H in the water molecules

67 through the notation δ:

68
$$\delta^{18}O = \left(\frac{\left(^{18}O / _{16}O \right)_{Sample}}{\left(^{18}O / _{16}O \right)_{VSMOW}} - 1 \right) \times 1000 \quad \text{(Eq. 1)}$$

69
$$\delta D = \left(\frac{\left(D / H \right)_{Sample}}{\left(D / H \right)_{VSMOW}} - 1 \right) \times 1000 \quad \text{(Eq. 2)}$$

70

71 where VSMOW (Vienna Standard Mean Ocean Water) is an international reference standard

72 for water isotopes.

73 There are two types of isotopic fractionation: equilibrium fractionation, which is caused by the

74 difference in saturation vapor pressure of different isotopes, and non-equilibrium fractionation,

75 which occurs due to molecular diffusion (e.g. during ocean evaporation in undersaturated

76 atmosphere or snowflakes condensation in oversaturated atmosphere). In the water vapor above

77 the ocean, the proportion of non-equilibrium fractionation, and hence diffusive processes can

78   be estimated by the deuterium excess, a second order isotopic variable denoted d-excess,

79   defined as (Dansgaard, 1964):

80

81                    $d\text{-excess} = \delta D - 8 \times \delta^{18}O$ (Eq.3)

82

83   Over the recent years and thanks to the development of optical spectroscopy enabling

84   continuous measurements of water isotopes ratios in water vapor, an increasing number of

85   studies have focused on the use of stable isotopes in water vapor to document the dynamic of

86   the water cycle over synoptic weather events, such as cyclones, cold fronts, atmospheric rivers

87   (Tremoy et al., 2014; Aemisegger et al., 2015; Munksgaard et al., 2015; Dütsch et al., 2016;

88   Graf et al., 2019; Lee et al., 2019; Ansari et al., 2020; Bhattacharya et al., 2022) or water cycle

89   processes such as water cycle processes such as evaporation over the ocean or deep convection

90   (Bonne et al., 2019; Benetti et al., 2015). For this objective, several instruments have been

91   installed either in observatory stations (e.g. Tremoy et al., 2012; Guilpart et al., 2017; Steen-

92   Larsen et al., 2013; Leroy-Dos Santos et al., 2020; Aemisegger et al., 2012) or on boat (e.g.

93   Thurnherr et al., 2019; Benetti et al., 2014). In the aforementioned studies, the interpretation of

94   the isotopic records is often performed using a hierarchy of isotopic models, from conceptual

95   models (Rayleigh type) to general circulation models or regional weather prediction models

96   equipped with water isotopes (Risi et al., 2010; Werner et al., 2011; Ciais and Jouzel, 1994;

97   Markle and Steig, 2022). Such data comparison enables one to test the performances of the

98   models either in the simulation of the dynamic of the atmospheric water cycle or in the

99   implementation of the water isotopes.

100   Our study is part of these dynamics analyses and aims at improving the documentation of

101   climate and water cycle in the Southern Indian Ocean. This region is poorly documented with

102   present-day observations despite its primary importance in governing CO_2 sinks. Moreover, we

103   lack precise descriptions of atmospheric processes associated with cloud microphysics and

104   surface-atmosphere exchange in polar regions, and the evolution of westerly wind locations and

105   strength (Fogt and Marshall, 2020).

106   Over the previous years, we have installed 3 water vapor analyzers on Reunion Island at the

107   Maïdo observatory (21.079°S, 55.383°E, 2160m) (Guilpart et al., 2017) and in Antarctica

108   (Dumont d'Urville and Concordia; (Leroy-Dos Santos et al., 2021; Bréant et al., 2019; Casado

109   et al., 2016) These instruments have been used for the following purposes. They document the

110   diurnal variability of the isotopic signal with the influence of the subtropical westerly jet on the

111   water isotopic signal at night as well as the cyclonic activity in La Réunion. In Antarctica, the

112   instruments have shown a strong influence of katabatic winds on the isotopic composition of

113   the water vapor (Bréant et al., 2019). In order to complete the picture of the atmospheric water

114   cycle over the Indian basin of the Southern Ocean already documented by these three analyzers,

115   we installed a new water vapor isotopic analyzer in the mid-latitude of the south Indian Ocean

116   on Amsterdam Island in November 2019.

117   The objective of this study is to provide the first analyses of isotopic records (vapor and

118   precipitation) in Amsterdam Island, with a comparison of meteorological data and

119   environmental data collected in parallel on the Amsterdam Island Observatory (e.g.

120   atmospheric mercury) to help interpretation of isotopic records. This study includes analyses of

121   meteorological maps, back trajectories as well as outputs from general circulation models

122   equipped with water isotopes. After a description of the different records over the years 2020

123   and 2021, model simulations and back trajectory methodology, we focus on some low-pressure

124   events (cold fronts) associated with a strong negative excursion of the $\delta^{18}O$ of water vapor over

125   a few days. These events, expressed strongly in the water vapor isotopic record, are then used

126   for evaluation of general circulation models equipped with water isotopes.

127

128   **2. Methods**

129   **2.1 Site**

130   Labelled a GAW WMO (Global Atmosphere Watch World Meteorological Organization)

131   global site, Amsterdam Island (37.7983◦ S, 77.5378◦ E) is a remote and very small island of 55

132   km^2 with a population of about 30 residents, located in the southern Indian Ocean at 3300 km

133   and 4200 km downwind from the nearest lands, Madagascar and South Africa, respectively

134   (Sprovieri et al., 2016). Climate is temperate, generally mild with frequent presence of clouds.

135   Seasonal boundaries were defined as follows: winter from July to September and summer from

136   December to February, in line with previous studies (Sciare et al., 2009). Average temperature

137   is lower in winter compared to summer (10°C vs 15°C) while relative humidity and wind speed

138   remain high (respectively 50-85% and 5 to 15 m s^{-1}) most of the year without a clear seasonal

139   cycle.

140   Numerous atmospheric compounds and meteorological parameters are and were continuously

141   monitored at the site from 1960 (Gaudry et al., 1983; Polian et al., 1986; Gros et al., 1999, 1998;

142   Sciare et al., 2000, 2009; Angot et al., 2014; Slemr et al., 2015; El Yazidi et al., 2018; Slemr et

143   al., 2020). In particular, the Amsterdam (AMS) site hosts several dedicated atmospheric

144   observation instruments notably at the Pointe Bénédicte atmospheric observatory (70 m above

145 sea level) where greenhouse gases (GES) concentration and mercury (Hg) species are

146 monitored (service ICOS-France Atmosphère, ICOS-AMS-416 IPEV program, GMOStral-

147 1028 IPEV program). Both GES and Hg species measurements respond to international

148 monitoring networks (ICOS – https://www.icos-cp.eu/, GEO-GOS4M –

149 http://www.gos4m.org/ for GES and Hg species respectively). CO_2, CO, CH_4 and Hg species

150 have been continuously measured since 1980, 2014, and 2012 respectively.

151
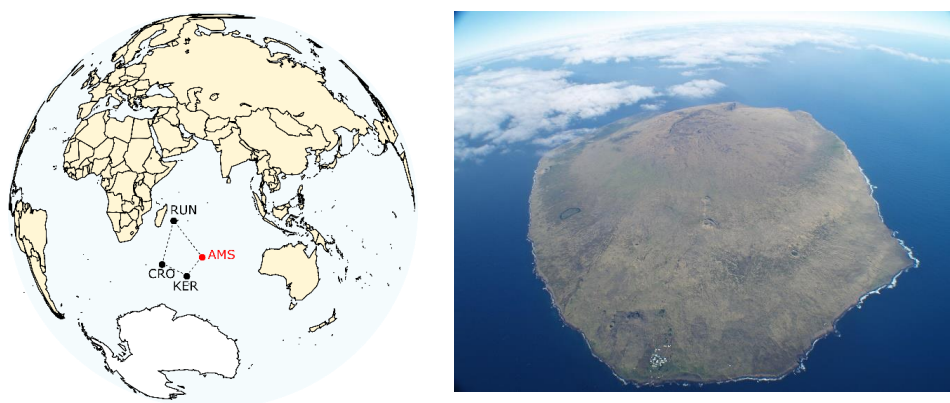
152

153 **Figure 1** : Location (left) and picture (right) of the Amsterdam Island. CRO: Crozet

154 Island; RUN: La Réunion island; KER: Kerguelen Island; AMS: Amsterdam Island.

155 Picture credit: left – Magand adapted from (Angot et al., 2016); right – Magand

156

157 **2.2 Long term measurements**

158 2.2.1 Meteorological measurements

159

160 Two meteorological stations are installed at the top of an observation mast (25 m above ground

161 level, agl) at the Pointe Bénédicte observatory (data used during this study), since 1980.

162 Installed and managed by ICOS-AMS-416 IPEV program, wind speed and direction,

163 atmospheric pressure, surface temperature and relative humidity are currently measured by a

164 WXT520 Vaisala weather system. Data (minute acquisition frequency) are cleaned and

165 processed by the IGE in the framework of the GMOStral-1028 IPEV program. Another

166 meteorological station is based on the island and is operated by Météo France at Martin-de-

167 Viviegs life base around 27 m above sea level, about two kilometers east from the Pointe

168 Bénédicte observatory. This second weather station collects air temperature, humidity,

169 precipitation, wind speed and direction, pressure and solar radiation via a mercury SYNOP

170 automatic weather station from STERELA meteo company. Only daily precipitation data

171 provided by Meteo France are used in the current study.

172

173 2.2.2 Gaseous elemental mercury (GEM)

174

175 Atmospheric GEM (Gaseous Elemental Mercury) measurements are conducted since 2012 in

176 the framework of IPEV GMOStral-1028 observatory program at the Pointe Benedicte

177 atmospheric research facility. Data are freely available on the national GMOS-FR data platform

178 AERIS ((Magand and Dommergue, 2022)) (https://gmos.aeris-data.fr, last access: 07/12/2022).

179 GEM is continuously measured (15 mn data frequency acquisition) using a Tekran 2537 A/B

180 instrument models (Tekran Inc., Toronto, Canada) (Angot et al., 2014; Slemr et al., 2015, 2020;

181 Sprovieri et al., 2016; Li et al., 2023). The operation device is based on mercury enrichment on

182 a gold cartridge, followed by a thermal desorption and a detection by cold vapor atomic

183 fluorescence spectroscopy (CVAFS) at 253.7 nm (Fitzgerald and Gill, 1979; Bloom and

184 Fitzgerald, 1988). Switching between two cartridges allows for alternating sampling and

185 desorption and thus results in a quasi-continuous temporal coverage of the mercury

186 measurement since the last decade. Concentrations are expressed in nanograms per cubic meters

187 at STP conditions (173.15 K and 1013.25 hPa) with an instrumental detection limit below

188 0.1 ng m^{-3} and a GEM average uncertainty value around 10% (Slemr et al., 2015). The

189 instrument is automatically calibrated following a strict procedure adapted from that of

190 Dumarey et al. (1985). Ambient air is sampled at 1.2 L min^{-1} through a heated (50°C) and UV

191 protected PTFE sampling line, with an inlet installed outside, 6 m agl. The air is filtered through

192 two 0.45 µm pore size polyether sulphone (PES) and one PTFE 47 mm diameter filters before

193 entering in the Tekran to prevent the introduction of any particulate material into the detection

194 system as well as capture any GOM (Gaseous Oxidised Mercury) or particulate bound mercury

195 (PBM) species ensuring that only GEM is sampled. To ensure the comparability of Hg

196 measurements around the world, the instrument is operated according to the Global Mercury

197 Observation System (GMOS) and CAMNET, AMNET standard operating procedures (Steffen

198 et al., 2012; Sprovieri et al., 2016). The detailed quality assurance and quality control required

199 by GMOS to produce qualified dataset are described in detail in the GMOS-FR data products

200 section in GMOS-FR website data portal (https://gmos.aeris-data.fr last access: 07/12/2022).

201 In this study, atmospheric GEM is used as potential tracer of intrusion and/or subsidence of

202 high altitude air masses (lower/ upper troposphere, or even above) that may possibly impact the

203   atmospheric records in Pointe Benedicte Observatory which collects marine boundary layer

204   most of the time (Angot et al., 2014 ; Sprovieri et al., 2016 ; Slmer et al., 2015, 2020). As

205   mentioned above, mercury in the atmosphere is detected in three defined forms: GEM, GOM

206   (HgO, $HgCl_2$, $HgBr_2$, $Hg[OH]_2$) and PBM. GEM, the dominant form of atmospheric mercury

207   species, is ubiquitous in the atmospheric reservoir and originates from a multitude of

208   anthropogenic and natural sources (Gaffney et al., 2014 ; Gworek et al., 2020 ; Gustin et al.,

209   2020 ; Edwards et al., 2021). Near the surface (marine or terrestrial boundary layer) and out of

210   polar regions, GOM and PBM represent only a few percent of the total atmospheric mercury

211   (Swartzendruber et al., 2006 ; Gustin and Jaffe, 2010 ; Gustin et al., 2015). Even if chemical

212   cycling and spatiotemporal distribution of mercury in the air, whatever atmospheric layer

213   considered (surface, mixed or free troposphere, stratosphere), is still poorly understood and

214   complete GEM oxidation schemes remain still unclear (Shah et al., 2021 and associated

215   references), several studies provided evidence that vertical distribution of atmospheric mercury

216   measurements from boundary layer to lower/upper troposphere and stratosphere shows a

217   decreasing trend in GEM concentration with increasing altitude, in parallel with an increase in

218   the concentration of divalent mercury (GOM + PBM) resulting from GEM oxidation

219   mechanisms (Murphy et al., 2006 ; Swartzendruber et al., 2006, 2008 ; Talbot et al., 2007 ; Fain

220   et al., 2009 ; Sheu et al., 2010 ; Lyman and Jaffe, 2012 ; Brooks et al., 2014 ; Fu et al., 2016 ;

221   Koenig et al., 2023). The identification of such observational processes (lower GEM

222   concentrations in high-altitude air masses versus marine boundary layer ones) is used here to

223   help characterizing possible high altitude air masses excursion in low altitude Pointe Benedicte

224   Observatory.

225

226   **2.3 Water vapor isotopic measurements**

227

228   The isotopic composition of near-surface water vapor ($\delta^{18}O_v$ and δD_v in ‰ versus SMOW) and

229   the water vapor mixing ratio (q_v in ppmv) have been measured continuously since November

230   2019. The measurements have been done with a Picarro Inc. instrument (L2130-I model) based

231   on wavelength-scanned cavity ring down spectroscopy. The instrument has been installed in a

232   temperature-controlled room at the observatory on the Amsterdam Island and the sampling of

233   water vapor is done outside at ~ 6 m above ground level.

234
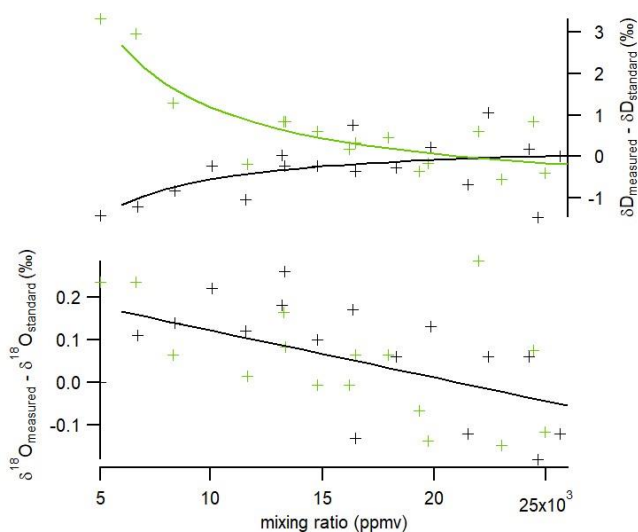
Figure 2: Dependency of δD (top) and δ18O (bottom) (anomaly from the true value of the standard) on the mixing ratio. The results are shown for two different standards (GREEN_AMS in green and EPB_AMS in black). The crosses indicate the data obtained with the set-up and the solid lines are the best regression curves (same curves for δ18O for both standards).

The calibration of the data is performed in different steps following previous studies (Tremoy et al., 2011; Leroy-Dos Santos et al., 2020). First, we quantified the influence of water vapor mixing ratio on the water isotope ratios. This effect is large at very low humidity (Leroy-Dos Santos et al., 2021). It can also depend on the isotopic composition of the standard water (Weng et al., 2020). Here, we introduced two different water standards, EPB-AMS and GREEN-AMS, with respective values of (-5.66 ‰, -47.31 ‰) and (-32.65 ‰, -263.76 ‰) for the couple (δ18O, δD) which encompass the isotopic values on site observations. The δ18O measurements of both EPB-AMS and GREEN-AMS standards decrease with increasing humidity with the same amplitude. In contrast, the δD measurements of both EPB-AMS and GREEN-AMS standards exhibit different behavior: δD of EPB-AMS increases by 1.5‰ and δD of GREEN-AMS decreases by 2.5 ‰ over the same 6,000-24,000 ppmv range for mixing ratio q_v.

As a consequence, the raw $\delta^{18}O_v$ measurements are corrected with the following regression:

$$\delta^{18}O_{v,corr} = \delta^{18}O_{v,measured} + 1.1.10^{-5} \times q + 0.232 \qquad \text{(eq 4)}$$

257

258 For the correction of the raw δD_v, we use two different regression splines for EPB-AMS and

259 GREEN-AMS (cf Figure 2):

260

261 $$\delta D_{EPB-AMS,corr} = \delta D_{EPB-AMS,measured} + \frac{9300}{q} - 0.383 \qquad \text{(eq 5)}$$

262 $$\delta D_{GREEN-AMS,corr} = \delta D_{GREEN-AMS,measured} - \frac{22400}{q} + 1.05 \qquad \text{(eq 6)}$$

263

264 The raw δD_v are thus weighted-corrected according to their distance of the measured δD

265 value from the EPB_AMS and the GREEN_AMS as follows:

266

267

268 $$\delta D_{v,corr} = \delta D_{GREEN-AMS,corr} + \frac{\delta D_{v,measured} - \delta D_{GREEN-AMS,measured}}{\delta D_{EPB-AMS,measured} - \delta D_{GREEN-AMS,measured}} \times (\delta D_{EPB-AMS,corr} - \delta D_{GREEN-AMS,corr})$$

269 $$\text{(eq 7)}$$

270

271 The second calibration step consists in the injection of the same two isotopic standards every

272 47 h at a mixing ratio of 13,000 ppmv to correct for any long-term drift. The correction

273 associated with this drift is less than 0.4 ‰ for $\delta^{18}O$ and 2.5 ‰ for δD over the two years of

274 measurements.

275 Precipitation were also sampled on a weekly basis in a rain gauge filled with paraffin oil which

276 permits to have measurements of water isotopic composition in the precipitation on a weekly

277 basis. The water samples are then sent for analyses at LSCE and measured on an isotopic

278 analyzer L2130-I by Picarro. The uncertainty associated with this series of measurements is of

279 ±0.15 ‰ for $\delta^{18}O$ and ±0.7 ‰ for δD leading to a quadratic error of ±1.4 ‰ for d-excess.

280

281 **2.4 Back trajectories: FLEXPART**

282

283 The origin and trajectory of air masses were assessed by FLEXPART, which is a Lagrangian

284 particle dispersion model (Pisso et al., 2019). All the meteorological data used to simulate the

285 back trajectories are taken from the ERA5 atmospheric reanalysis (Hersbach et al., 2020) with

286 a 6-hourly resolution. The ERA5 reanalysis is carried out by the European Center for Medium-

287 Range Weather Forecasts (ECMWF), using ECMWF's Earth System model IFS (Integrated

288 Forecasting System), cycle 41r2. For a few selected events, FLEXPART calculated

289 back trajectories over 10 days with 1000 launches of neutral particles (sensitivity test) of inert

290 air tracers released randomly (volume of 0.1°×0.1°×100 m) every 3 hours at 100 m altitude

291 above sea level (Leroy-Dos Santos et al., 2020), centered around the coordinates of Amsterdam

292 Island. The results of FLEXPART back trajectories are then displayed in particle density

293 probability.

294 **2.5 General atmospheric circulation model equipped with water stable**

295 **isotopes**

296

297 **2.5.1 LMDZ-iso model**

298

299 LMDZ-iso (Risi et al., 2010) is the isotopic version of the atmospheric general circulation

300 model LMDZ6 (Hourdin et al., 2020). We have used LMDZ-iso version 20230111.trunk with

301 the physical package NPv6.1, identical as the atmospheric setup of IPSL-CM6A (Boucher et

302 al., 2020) used for phase 6 of the Coupled Model Intercomparison Project (CMIP6, (Eyring et

303 al., 2016)). We performed two simulations, one at very low horizontal resolution (VLR, 3.75°

304 in longitude and 1.9° in latitude, 96×95 grid cells) and the second at low horizontal resolution

305 (LR, 2.0° in longitude and 1.67° in latitude, 144×142 grid cells). Both simulations have 79

306 vertical levels and the first atmospheric level is located around 10 m above ground level. The

307 LMDZ-iso 3D-fields of temperature and wind are nudged toward the 6-hourly ERA5 reanalysis

308 data with a relaxation time of 3 hours. Surface ocean surface boundary conditions are taken

309 from the monthly mean SST and sea-ice fields from the CMIP6 AMIP Sea Surface Temperature

310 and Sea Ice dataset version 1.1.8 (Durack et al., 2022; Taylor et al., 2000). LMDZ-iso outputs

311 are used at a 3-hourly resolution. The Amsterdam Island (58 km²) is too small to be represented

312 in the LMDZ-iso model.

313

314

315 **2.5.2 ECHAM6-wiso model**

316

317 ECHAM6-wiso (Cauquoin et al., 2019; Cauquoin and Werner, 2021) is the isotopic version of

318 the atmospheric general circulation model ECHAM6 (Stevens et al., 2013). The

319 implementation of the water isotopes in ECHAM6 has been described in detail by Cauquoin et

320 al. (2019), and has been updated in several aspects by Cauquoin and Werner (2021) to make

321 the model results more consistent with the last findings based on water isotope observations

322   (isotopic composition of snow on sea ice considered, supersaturation equation slightly updated,

323   and kinetic fractionation factors for oceanic evaporation assumed as independent of wind

324   speed). We have used ECHAM6-wiso model outputs from a simulation at T127L95 high spatial

325   resolution (0.9° horizontal resolution and 95 vertical levels) nudged to ERA5 reanalysis

326   (Hersbach et al., 2020). ECHAM6-wiso is thus run with a finer resolution than both LMDZ-iso

327   simulations. The ECHAM6-wiso 3D-fields of temperature, vorticity and divergence as well as

328   the surface pressure field were nudged toward the ERA5 reanalysis data every 6 hours. The

329   orbital parameters and greenhouse gases concentrations have been set to the values of the

330   corresponding model year. The monthly mean sea surface temperature and sea-ice fields from

331   the ERA5 reanalysis have been applied as ocean surface boundary conditions, as well as a mean

332    $\delta^{18}O$ of surface seawater reconstruction from the global gridded data set of (LeGrande and

333   Schmidt, 2006). As no equivalent data set of the δD composition of seawater exists, the δD of

334   the seawater in any grid cell has been set equal to the related $\delta^{18}O$ composition, multiplied by

335   a factor of 8, in accordance with the observed relation for meteoric water on a global scale

336   (Craig, 1961). The ECHAM6-wiso simulation is described in detail and evaluated in Cauquoin

337   and Werner (2021). ECHAM6-wiso outputs are given at a 6-hourly resolution. As for the

338   LMDZ-iso model, the Amsterdam Island (58 km^2) is too small to be represented by ECHAM6-

339   wiso.

3. Results

3.1 Data description
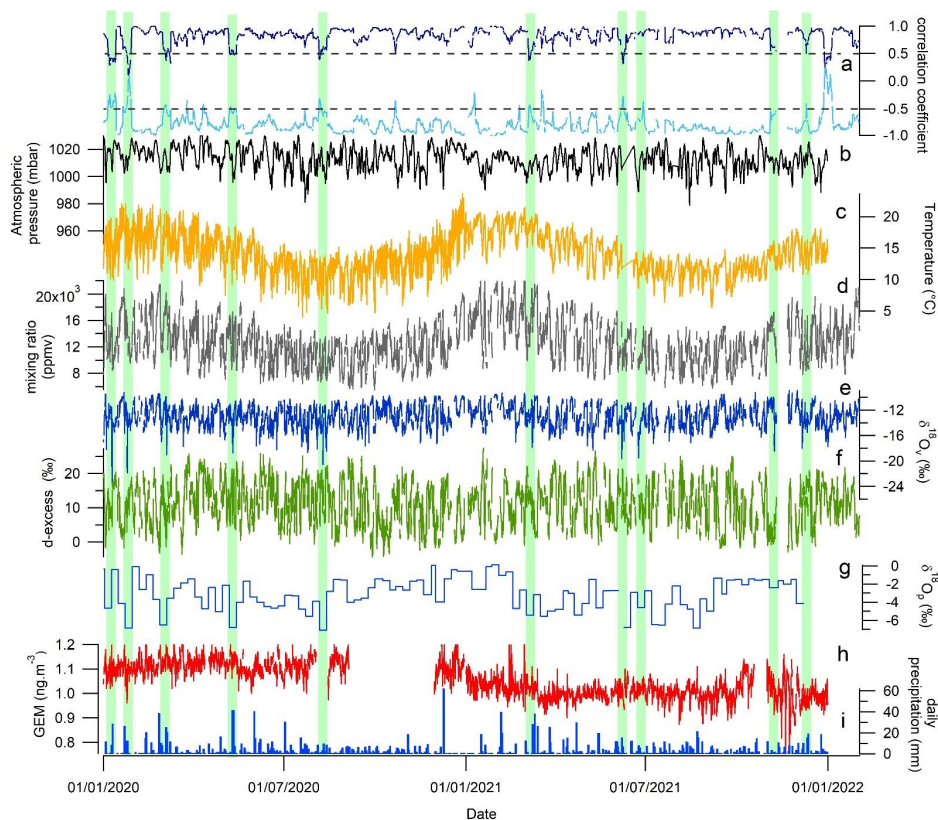
Figure 3 : Meteorological, isotopic and GEM records for the years 2020 and 2021 on the Amsterdam Island : (a) correlation coefficient between water vapor $\delta^{18}O$ and mixing ratio (dark blue, top) and between water vapor $\delta^{18}O$ and d-excess (light blue, bottom) over a moving time window of 8 days, (b) atmospheric pressure (hourly average), (c) atmospheric temperature (hourly average), (d) mixing ratio (hourly average), (e) $\delta^{18}O$ of water vapor (hourly average), (f) d-excess of water vapor (hourly average), (g) $\delta^{18}O$ of precipitation sampled on a weekly basis, (h) GEM concentration, (i) daily precipitation. The green rectangles indicate the period with (1) correlation coefficient >-0.5 between d-excess and $\delta^{18}O$ of water vapor and (2) occurrence of a negative excursion in water vapor $\delta^{18}O$.

13

3.1.1 Temporal variability in the meteorological records

As mentioned earlier, there is a clear annual cycle at Amsterdam Island as recorded in the temperature and water mixing ratio for the years 2020 and 2021. The December-February period (austral summer) has the highest temperatures with an average of 15.0°C, while in winter (July-September) the average temperature varies around 10.5°C. In parallel, we do not see clear patterns of a diurnal cycle except for some periods in the temperature records yet with a small amplitude (4-5 °C).

The impact of synoptic events at the scale of a few days is visible in the temperature and water mixing ratio with a covariation of temperature and water mixing ratio with amplitude of up to 10°C in temperature and more than 10,000 ppmv in water mixing ratio.

3.1.2 Temporal variability in the GEM record

Previous studies clearly showed that AMS is little influenced by anthropogenic sources of Hg, and greatly influenced by the ocean surrounding the island (Angot et al., 2014; Slemr et al., 2015, 2020; Jiskra et al., 2018; Li et al., 2023; Hoang et al., 2023). Angot et al., (2014) reported mean annual GEM concentrations of about 1.03 ± 0.08 ng m^{-3} from 2012 to 2013. These concentrations are ~30% lower than those measured in remote sites of the northern hemisphere. Over the period 2012 to 2017, Slmer et al. (2020) confirmed that higher GEM concentrations can be found during austral winter. Lower GEM values are generally observed in October and November, as well as in January and February during austral summer. Using this 6-yr long data set, mean annual GEM concentration was 1.04 ± 0.07 ng m^{-3} (annual range: 1.014 to 1.080 ng m^{-3}) i.e. very close to the one observed in Angot et al (2014).

During the period (2020-2021) of water vapor isotope measurements in AMS, GEM showed mean annual concentration in the range of 1.11 ± 0.04 ng m^{-3} and 1.00 ± 0.04 ng m^{-3}, for years 2020 and 2021 respectively, slightly higher and lower than the ones observed in previous mentioned studies. Surprisingly, unlike the 2012-2017 data set, GEM presented in this study did not show a significant higher mean concentration during the austral winter months than during the summer months (Figure 3), with consequently no discernible seasonal amplitude of GEM. On a finer timescale, the lack of a clear pattern of GEM seasonal cycle is counterbalanced by days showing abrupt increases or decreases in concentrations. Some of the sudden GEM decreases (until more than 15 % of the concentration in few hours, i.e. up to 0.15-0.20 ng m^{-3} difference) appear concomitant with important negative peak of several ‰ in water vapor δ^{18}O.

### 3.1.3 Temporal variability of water isotopic composition

14

386   The isotopic composition of precipitation ($\delta^{18}O_P$) sampled on a weekly basis displays a quite

387   large variability ($\delta^{18}O_P$ = -3.06 ± 1.75 ‰, n=104) with values slightly higher during austral

388   summer (difference between summer and winter $\delta^{18}O_P$ values is about 2 to 3 ‰) (Figure 3). No

389   significant seasonal variations are observed in the record of d-excess of the precipitation.

390   No diurnal cycle can be detected in the $\delta^{18}O_v$ and d-excess$_v$. The annual cycles are also not

391   visible (1 ‰ difference between summer and winter mean $\delta^{18}O_v$ value while standard deviation

392   of the entire record at 1 h resolution is 1.7 ‰). Only the synoptic scale variability is well

393   expressed in the records of $\delta^{18}O_v$ and d-excess$_v$ with an anticorrelation between both parameters

394   when looking at the 2-year series at hourly resolution (R^2 = 0.61). Moreover, water vapor $\delta^{18}O$

395   is most of the time correlated with water mixing ratio (R^2 = 0.55 for the 2-year series at hourly

396   resolution).

397   There are a few exceptions to the general correlation between water vapor $\delta^{18}O$ and mixing

398   ratio as illustrated on Figure 3. Short periods of a few days are associated with a decrease of

399   the correlation coefficient, R, between $\delta^{18}O_v$ and q_v (R is calculated continuously from hourly

400   records in 8 consecutive days). The periods of decreased R are also characterized by a negative

401   peak of several ‰ in $\delta^{18}O_v$, which are not visible in the d-excess$_v$. During these $\delta^{18}O_v$

402   excursions occurring during cold fronts, the general anti-correlation between $\delta^{18}O_v$ and d-

403   excess$_v$ hence also breaks down. Our study mostly focuses on the 11 abrupt events highlighted

404   by the water vapor $\delta^{18}O$ record (only 10 visible on Figure 3 because of the scale).

405

406   **3.2 Model-data comparison**
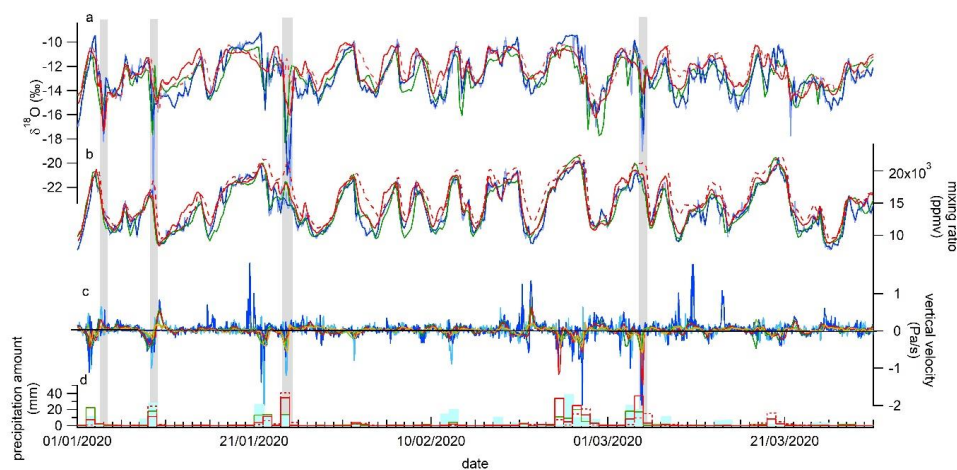
407

408   **Figure 4**: Data model comparison (January – March 2020) : water vapor $\delta^{18}O$ from our data

409   set (light blue on hourly average, dark blue resampled at a 6-hour resolution), the ECHAM6-

410   wiso model (green, surface level, 6h resolution) and the LMDZ-iso model (red, surface level,

411   3h resolution) at very low resolution (VLR, dashed line) and at low resolution (LR, solid line)

412   (a) ; mixing ratio from our data set (light blue on hourly average, dark blue resampled at a 6

413   hours resolution), the ECHAM6-wiso model (green, surface level, 6h resolution) and the

414   LMDZ-iso model (red, surface level, 3h resolution, dashed line for VLR and solid line for LR)

415   (b) ; vertical velocity from the ERA5 reanalyses (500 hPa, blue, 850 hPa, light blue), from the

416   ECHAM6-wiso model (500 hPa, green, 850 hPa, light green), from the LMDZ-iso model at LR

417   (500 hPa, red, 850 hPa, orange) (c) ; Precipitation amount from the meteorological record in

418   light blue, from the ECHAM6-wiso model in green and from the LMDZ-iso model in red

419   (dashed line VLR and solid line LR) (d). The grey rectangles highlight the negative $\delta^{18}O$

420   excursions (note that in this figure the excursions of the 3rd and 9th of January 2020 are distinct

421   while the distinction could not be done on Figure 3 because of the scale).

422

423   We selected a 3-month period (January to March 2020) for the comparison between our set of

424   data and the outputs of the ECHAM6-wiso and LMDZ-iso models. This period has been

425   selected for display because it encompasses 4 out the 11 negative excursions of $\delta^{18}O_v$, but the

426   extended comparison over the whole 2 years period is displayed on Figure S1. There is an

427   overall agreement between the measured and modelled water vapor $\delta^{18}O$ and mixing ratio

428   (Figure 4). The best agreement over the 3-month series is obtained with the ECHAM6-wiso

429   and LMDZ-iso (LR) models ($R^2 = 0.59 – 0.6$ and $0.87 - 0.90$ respectively for $\delta^{18}O_v$ and mixing

430   ratio series) while a slightly less good agreement is observed with the VLR simulation of the

431   LMDZ-iso model ($R^2 = 0.49$ and 0.79 respectively for $\delta^{18}O_v$ and mixing ratio series). The same

432   observation can be done on the entire two-year series. We also compare the precipitation

433   amount modelled by ECHAM6-wiso and LMDZ-iso to the precipitation amount measured by

434   the MeteoFrance weather station and in general, the agreement with measured precipitation

435   amount is better for ECHAM6-wiso ($R^2 = 0.45$) than for LMDZ-iso ($R^2 = 0.08 – 0.13$ for VLR

436   - LR). Finally, when focusing on the 4 short term negative excursions of the water vapor $\delta^{18}O$

437   (grey rectangles in Figure 5), they are in general more strongly expressed in the data series than

438   in the model series which is only partly due to the hourly resolution of the $\delta^{18}O_v$ record

439   compared to the 3h and 6h resolution of the outputs of the LMDZ-iso and ECHAM6-wiso

440   models respectively (Figure 4 red dashed and solid lines on panel c and Table 1 9th column).

441 When looking at the whole two-year series, the LMDZ-iso VLR simulation fails to reproduce

442 most of these excursions (only the negative excursion of the 3rd of January 2020 is reproduced)

443 while the ECHAM6-wiso model is able to capture all the excursions. The LMDZ-iso LR

444 simulation produces a negative $\delta^{18}O_v$ excursion over many events but significantly less

445 expressed than in the data and in the ECHAM6-wiso model (Table 1).

446

447 **4. Discussion**

448 The most remarkable pattern from this two-year series is the succession of short negative

449 excursions of $\delta^{18}O_v$ associated with decorrelation between $\delta^{18}O_v$ and humidity, $\delta^{18}O_v$ and d-

450 excess$_v$ and highlighted with green rectangles in Figure 3 and referenced in Table 1. They

451 always occurred during low pressure periods (atmospheric pressure below 1005 mbar). The

452 focus on the first three months of the series presented on Figure 4 shows that these events are

453 captured by ECHAM-wiso at 0.9° resolution, but not systematically by LMDZ-iso at 2x1.67°

454 and even less by LMDZ-iso at 3.75x1.9° resolution. Such mismatch makes the understanding

455 of the processes at play during these events particularly important to test and improve the

456 performances of atmospheric general circulation models equipped with water isotopes.
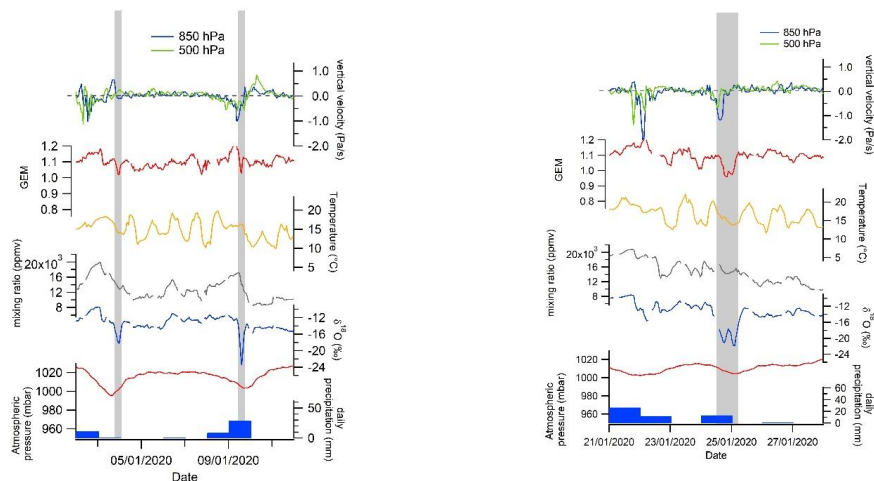
457

458 **Figure 5 :** Evolution of GEM, water vapor $\delta^{18}O$, mixing ratio, meteorological parameters

459 (surface temperature, surface atmospheric pressure, daily precipitation) measured by the

460 MeteoFrance weather station and vertical velocity from the ERA5 reanalyses at 500 and 850

461 hPa over the three isotopic excursions of January 2020 identified on Figure 4.

462

463 **Table 1**: List of the cold front events associated with both loss of correlation between $\delta^{18}O_v$

464 and q_v, $\delta^{18}O_v$ and d-excess$_v$ and negative excursions of $\delta^{18}O_v$ over 2020-2021. The length of

465 the event is estimated from the time difference between the mid slope of the $\delta^{18}O_v$ decrease at

466 the beginning of the event and the mid-slope of the $\delta^{18}O_v$ increase at the end of the event. The

467 amplitude of the negative $\delta^{18}O_v$ anomaly is calculated between the average $\delta^{18}O_v$ level 24h

468 before and 24h after the excursion and the minimum of $\delta^{18}O_v$ on the record at hourly resolution

469 (at 6h resolution). When the calculated amplitude is smaller than 1 ‰, we indicate only "-".

470 When the vertical velocity is between -0.25 and 0.25 Pa/s, we indicate "~0".

471

Date of the event	Negative excursion of GEM	Low pressure (< 1005 mbar)	Rain	Relative Humidity at the surface	vertical velocity from reanalyses (850 hPa)	vertical velocity from reanalyses (500 hPa)	Lenth of the event (hours)	amplitude of the $\delta^{18}O$ peak in the data (‰)	amplitude of the $\delta^{18}O$ peak in ECHAM-wiso (‰)	amplitude of the $\delta^{18}O$ peak in LMDZ-iso VLR (‰)	amplitude of the $\delta^{18}O$ peak in LMDZ-iso LR (‰)
06/12/2021	Yes	Yes	Yes	82%	~0	up	3h	-6 (-5)	-2.3	-	-2
08/11/2021	Yes	Yes	No	85%	~0	~0	17h	-5.5 (-5.5)	-5	-	-4
23/06/2021	No	Yes	Yes	75%	~0	~0	10h	-5.5 (-5.4)	-6	-	-
07/06/2021	No	Yes	Yes	80%	up	~0	9h	-6.5 (-5.8)	-5.8	-	-2
08/03/2021	Yes	Yes	Yes	89%	down	up	20h	-6 (-6)	-4	-	-
09/08/2020	No data	Yes	Yes	87%	down	up	8h	-8 (-6)	-7	-	-2
10/05/2020	Small	Yes	Yes	95%	down	down	14h	-4.9 (-4)	-3	-	-3
04/03/2020	No data	Yes	Yes	98%	Up	Up	9h	-6.1 (-5.3)	-5	-	-
24/01/2020 (double peak)	Yes	Yes	Yes	93% and 90%	1st peak up and 2nd peak down	1st peak up and 2nd peak down	17h	-7.8 (-7.5)	-4.5	-	-3.5
09/01/2020	Yes	Yes	Yes	94%	up	up	4h	-9 (-4)	-5	-	-
03/01/2020	Yes	Yes	No	90%	down	~0	6h	-2.8 (-2.5)	-2.4	-3	-3.5

472

473

474 Several hypotheses can be proposed to explain the negative excursions of water vapor $\delta^{18}O$

475 during cold front periods. The beginning of these excursions is associated with a decrease of

476 water mixing ratio and they occur in most cases (but not always) during a precipitation event

477 (Table 1). These events share similarities with the negative $\delta^{18}O_v$ and $\delta^{18}O_p$ short events

478 previously observed in temperate regions during a cold front passage (e.g. Aemisegger et al.,

479 2015). Three possible processes at play to explain such events were already listed in previous

480 studies (e.g. Dütsch et al., 2016) (i) local interaction between the vapor and the rain droplets

481 (rain equilibration and rain evaporation), (ii) vertical subsidence of water vapor with depleted

482 isotopic composition, or (iii) horizontal advection through the arrival of a cold front.

483
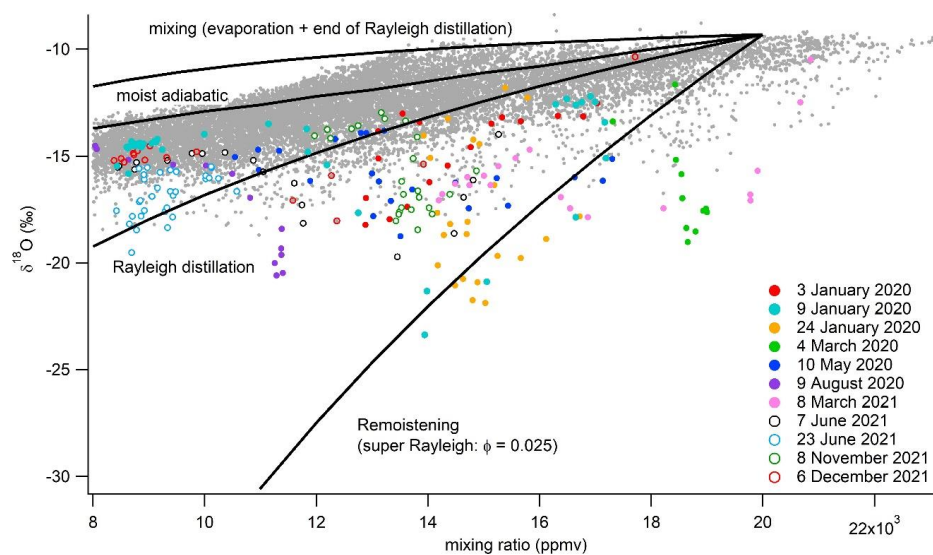
Figure 6: Evolution of the mixing ratio and isotopic composition of water vapor for the different events (colors according to the date as explained on the graph) and for the entire 2 years records (grey). The solid lines are theoretical lines inspired from (Noone, 2012) for different processes (remoistening associated with exchange between rain and water vapor; Rayleigh distillation assuming that all formed condensation is removed from the cloud; moist adiabatic process assuming that liquid condensation stays in the cloud with the water vapor; mixing of water vapor from ocean evaporation around Amsterdam Island and water vapor from the end of the Rayleigh distillation, i.e. high altitude water vapor). The water vapor for the calculation of Rayleigh distillation and for the evaporation above the ocean has a mixing ratio of 20,000 ppmv and a $\delta^{18}O_v$ of -9.3 ‰. The vapor at the end of the distillation line was taken with a mixing ratio of 1,000 ppmv and a $\delta^{18}O_v$ of -40 ‰.

We first explore how we can gain information on the different processes listed above from our data set. First, to test the hypothesis of vapor-droplet interactions, we looked at the $\delta^{18}O_v$ vs q_v distribution (Figure 6). In general, the $\delta^{18}O_v$ vs q_v evolution lies on a curve which can be explained by condensation processes (Rayleigh distillation or reversible moist adiabatic process). However, for the 11 events highlighted above, the $\delta^{18}O_v$ vs q_v evolution follows an evolution characteristic of remoistening processes, i.e. a curve standing below the curve of the $\delta^{18}O_v$ vs q_v evolution observed for the rest of the series, which demonstrates the depleting effect

19

504   of vapor-rain interactions (Worden et al., 2007; Noone, 2012). Since relative humidity is

505   relatively high during these events (values given in Table 1 compared to a mean value of 77 %),

506   it more likely reflects rain-vapor diffusive exchanges than rain evaporation.

507   Second, to test the hypothesis, of subsidence of air from higher altitude, GEM is used. Indeed,

508   aircraft measurements as well as model simulations demonstrated that the upper

509   troposphere/lower stratosphere (UTLS) is depleted in GEM and enriched in species composed

510   of reactive gaseous mercury and particulate bound mercury (Murphy et al., 2006;

511   Swartzendruber et al., 2006, 2008; Sillman et al., 2007; Talbot et al., 2007, 2008; Lyman and

512   Jaffe, 2012). This leads to lower GEM concentrations than those usually observed when the

513   lowest atmosphere layer is only under marine influence (Lindberg et al., 2007; Angot et al.,

514   2014). The fact that GEM negative excursions are observed in phase with negative $\delta^{18}O_v$

515   excursions in most of the events (7 events on a total of 9 events with GEM data, cf Figure 5,

516   Table 1) suggests that vertical subsidence of water vapor, $\delta^{18}O$-depleted by Rayleigh distillation

517   and/or rain-vapor interactions, can have an influence on the observed excursions of $\delta^{18}O_v$, in

518   agreement with the conclusion of Dütsch et al. (2016).

519   To further explore the processes leading to the decoupling of humidity and $\delta^{18}O_v$ as well as

520   sharp negative excursions of $\delta^{18}O_v$ during the 11 events identified here, we also use information

521   from the ERA5 reanalyses. In particular, the influence of atmospheric circulation (vertical and

522   horizontal advection) can be studied through back trajectories. The back trajectories (see some

523   examples in SI, Figures S2 and S3) confirm the information from wind directions that there is

524   no systematic change in the horizontal origin of the trajectories for the different events. On the

525   contrary, back trajectories clearly indicate a strong subsidence over some events, in particular

526   for the event of the 3rd of January: the maximum altitude of the envelope of the back trajectories

527   increases from 5,000 to 8,000 m when comparing the situation before the excursion and the

528   situation during the most negative water vapor $\delta^{18}O$ value, hence confirming the occurrence of

529   air subsidence indicated by the GEM record (Figure S2). A less clear but similar situation is

530   observed for the anomaly of the 24th of January 2020 which is associated with an increase of

531   the maximum altitude of the back trajectories from 4,000 to 6,000 m when comparing the

532   situation before the excursion and the situation corresponding to the most negative water vapor

533    $\delta^{18}O$ value. Back trajectories are however not supporting systematic subsidence for other cases

534   (e.g. event of the 9th of January, Figure S3).

535   The subsidence over the different events can also directly be followed on the vertical velocity

536   from the ERA5 reanalyses (Figure 4). Subsidence (positive vertical velocity) is not

537   systematically associated with negative $\delta^{18}O_v$ excursions: subsidence at either 850 hPa or 500

538   hPa is observed only for 5 events over 11 (Table 1). In 4 cases, there is rather an ascending

539   movement of the atmosphere associated with the rain event. In the other cases, there is no clear

540   vertical movement. However, we note that when negative $\delta^{18}O_v$ excursions are not concomitant

541   with subsidence, they occur right after an ascending movement and are generally followed by

542   subsidence (Figure S1).

543   The effect of change in horizontal air mass origin is difficult to study from our data. There is

544   no evidence for changes in the horizontal advection of air over the 11 particular events from

545   the observation of wind direction around these cold front events. The back trajectories permit

546   to look at a possible change of horizontal advection higher in the atmosphere. Again, no clear

547   change of horizontal advection at higher altitude is observed for the 11 events associated with

548   a sharp decrease of the $\delta^{18}O_v$.

549   With the information gathered above, both subsidence and isotopic depletion associated with

550   rain occurrence and further interaction between droplets and water vapor can explain the

551   negative excursion of $\delta^{18}O_v$. We note however that the data gathered so far do not permit to

552   provide a simple and unique explanation. Neither subsidence nor rain systematically occurred

553   for each of the $\delta^{18}O_v$ excursion. Still, the fact that at least ECHAM6-wiso is able to reproduce

554   every negative $\delta^{18}O_v$ excursions (whether they are associated or not with subsidence or rain-

555   water vapor reequilibration) shows that the atmospheric circulation patterns are correctly

556   reproduced and that the isotopic processes are correctly implemented in this model. Such abrupt

557      $\delta^{18}O_v$ events can hence be used as a test of the performances of general circulation models

558   equipped with water isotopes.

559   To better understand why the models are less able to reproduce the $\delta^{18}O_v$ excursions at coarser

560   resolution, we compare the performances of the ECHAM6-wiso and the LMDZ-iso models

561   over the first months of 2020 in term of atmospheric dynamic (the whole series is displayed in

562   SOM). First, the two models reproduce rather well the evolution of the vertical velocity from

563   the ERA5 reanalyses with a stronger ascent for the model predicting the strongest precipitation

564   amount (e.g. LMDZ-iso for 24th of January 2020). The event of the 3rd of January is the only

565   one reproduced by both ECHAM6-wiso and the two versions of the LMDZ-iso model: the three

566   simulations show a clear subsidence over the isotopic event and a clear negative $\delta^{18}O_v$ excursion

567   (Figure 4). For the other events, neither LMDZ-iso nor ECHAM6-wiso show a clear signal of

568   subsidence neither at 500 nor at 850 hPa (Figure 4). However, the horizontal distribution of

569   vertical velocity obtained with ECHAM6-wiso and LMDZ-iso are significantly different
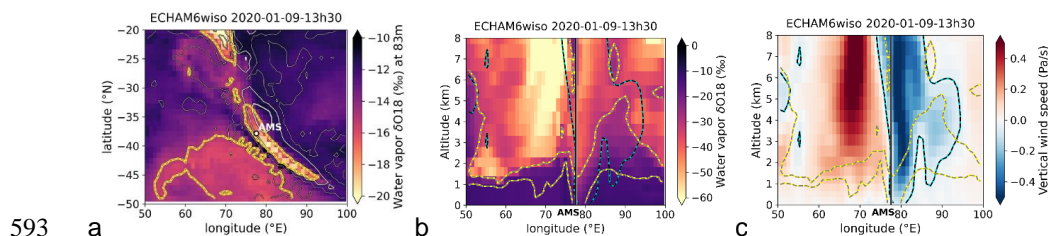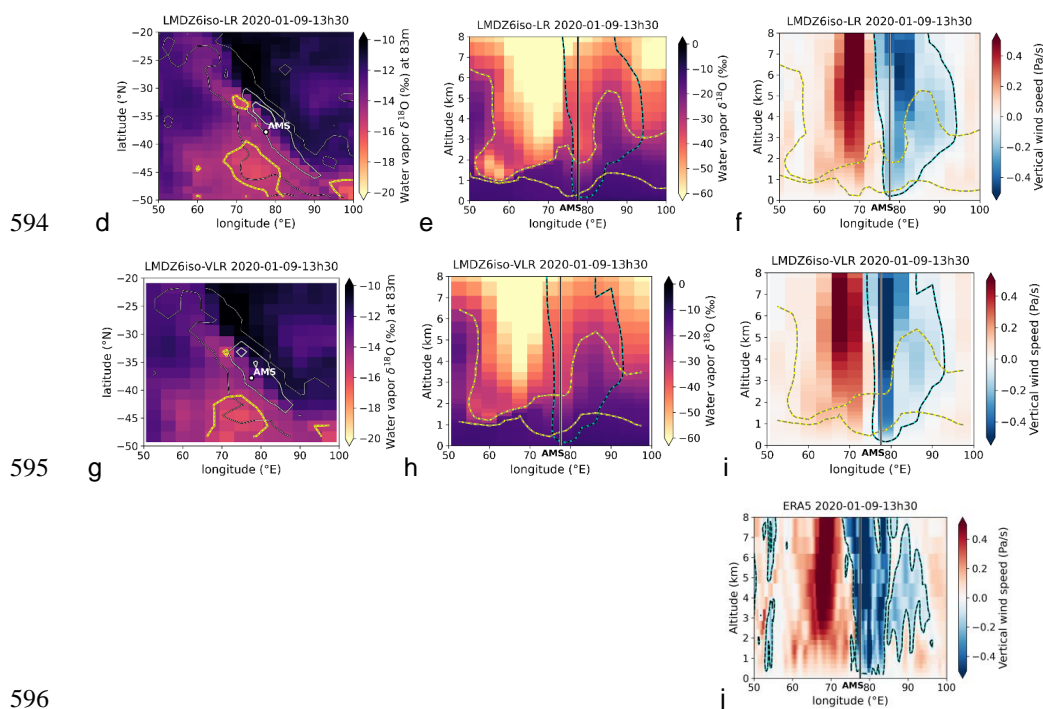
570 (Figure 7 for the event of the 9th of January, Figures S5 for the other events). While the LMDZ-

571 iso modelled vertical velocity displays a rather strong homogeneity on the vertical axis,

572 ECHAM6-wiso modelled vertical velocity highlights subsidence of air below the ascending

573 column at the exact location of the negative $\delta^{18}O_v$ anomaly (Figure 7c). This subsidence of

574 depleted $\delta^{18}O_v$ below the ascending column is responsible for the sharp negative $\delta^{18}O_v$

575 excursion in the ECHAM6-wiso model. The fact that subsidence of air occurs just below

576 uplifted air, at the limit between ascendance and subsidence (Figure 7j), permits to reconcile

577 the GEM data suggesting subsidence and the sign of the vertical velocity of the ERA5

578 reanalyses at Amsterdam Island. We propose that the reason why the LMDZ-iso model does

579 not reproduce well the water isotopic anomaly is its too coarse resolution. Indeed, Table 1 and

580 Figure 4 show that for the event of the 24th of January, the LMDZ-iso model at low resolution

581 is able to reproduce the isotopic anomaly while the LMDZ-iso model at very low resolution

582 fails. A fine resolution is necessary to capture the details of the spatial patterns of the vertical

583 velocity and $^{18}O_v$. Similar observations can be done on other events as shown in the SI (Figures

584 S5 to S11).

585 Figure 8 summarizes the proposed mechanism for negative $\delta^{18}O_v$ excursions as inferred from

586 our data – model comparison when there is a clear rain event. A rain event is associated with a

587 strong ascending column in which $\delta^{18}O_v$ is depleted by progressive precipitation during the

588 ascent and by interaction between rain and water vapor. This ascending column is coupled to

589 the subsidence of $\delta^{18}O_v$ depleted air at the rear of the event which is pushed toward Amsterdam

590 Island through a south west advection of cold air.

591

592

593 a   b   c

594

595

596

597

Figure 7: Evolution of the modelled $\delta^{18}O_v$ and vertical velocity over the event of the 9th of January 2020. (a) low level (~83 m) contourplot of $\delta^{18}O_v$ on a latitude vs longitude plot, the yellow line indicates the -15‰ level and grey contours indicate precipitation contours at 0.5, 10, and 50 mm day^{-1} (thin, medium and thick lines respectively); (b) $\delta^{18}O_v$ evolution on a altitude vs longitude plot, the yellow lines indicate the $\delta^{18}O_v$ levels at -30 and -15 ‰, the blue plot the contour of –0.05 Pa s^{-1} vertical velocity (ascendance) and the vertical black line denotes Amsterdam Island latitude; (c) vertical velocity evolution on an altitude vs longitude plot with similar lines as in (b) ; (a), (b) and (c) are drawn using outputs of the ECHAM6-wiso model ; (d), (e) and (f) are the same as (a), (b) and (c) but obtained from the LMDZ-iso model at low resolution (LR) ; (g), (h) and (i) are the same as (a), (b) and (c) but obtained from the LMDZ-iso model at very low resolution (VLR); (j) shows the vertical velocity on a altitude vs longitude plot from ERA5.
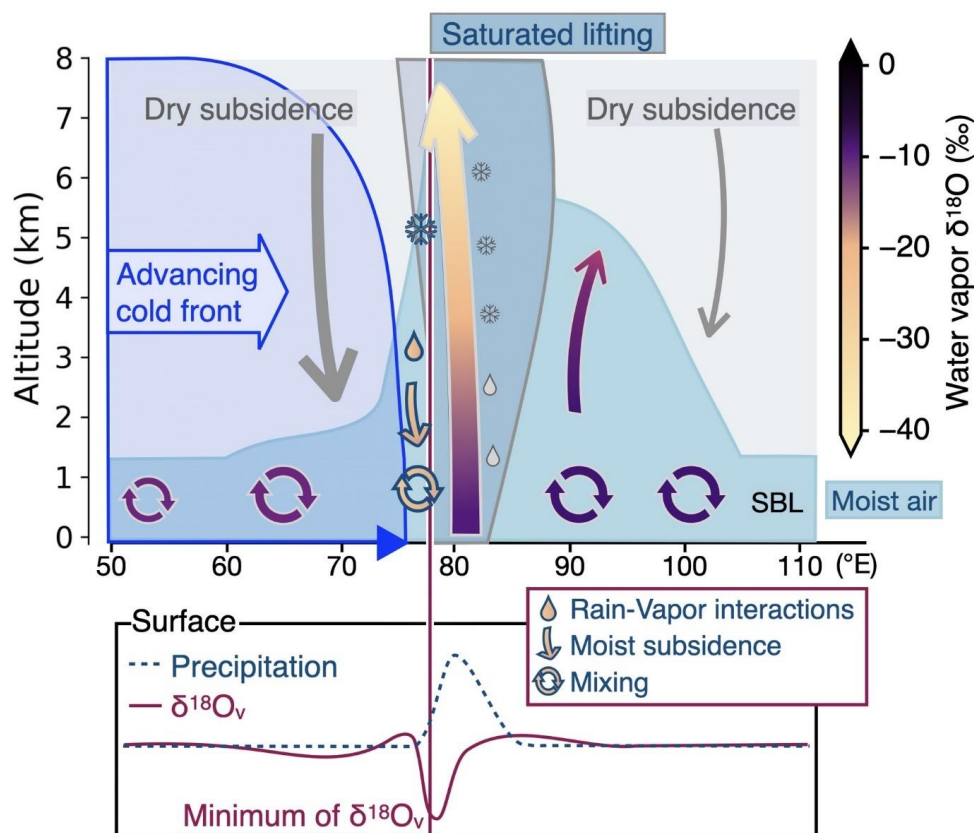
Figure 8: Scheme of the mechanism explaining the sharp negative excursion of $\delta^{18}O_v$ recorded at the surface for cold front events associated with precipitation. The top panel show the altitude vs longitude dynamics of air masses with vertical saturated lifting in the center and subsidence at the rear of the lifting. The bottom panel shows the associated evolution of $\delta^{18}O_v$ and precipitations on the same longitude scale than on the upper panel.

5. Conclusion

We presented here the first water vapor isotopic record over 2 years in Amsterdam Island. The water vapor isotopic variations follow at first order the variations of water mixing ratio as expected from a marine site. Superimposed to this variability, we have evidenced 11 periods of a few hours / days where the correlation between $\delta^{18}O_v$ and water mixing does not hold. These periods are associated with the occurrence of one or two abrupt negative excursions of $\delta^{18}O_v$. These negative excursions associated with cold fronts are often occurring toward the end of

624 precipitation events. They are characterized by a decrease in water mixing ratio. Representation

625 of these short events is a challenge for the atmospheric components of Earth System Models

626 equipped with water isotopes and we found that the ECHAM6-wiso model was able to

627 reproduce most of the sharp negative $\delta^{18}O_v$ excursions while the LMDZ-iso model at 2° (3°)

628 resolution was only able to reproduce 7 (1) of the negative excursions.

629 Using previous modeling studies as well as information provided by (1) confrontation with

630 other data sources (GEM, meteorology) obtained in parallel on this site, (2) back trajectory

631 analyses and (3) the outputs of the two models ECHAM6-wiso and LMDZ-iso, we conclude

632 that the most plausible explanations for such events are rain-vapor interactions and subsidence

633 at the rear of a precipitation event. Both can be combined, since rain vapor interactions can help

634 maintain moist conditions in subsidence regions.

635 This study highlighted the added value of combining different data from an atmospheric

636 observatory to understand the dynamic of the atmospheric circulation. The two-year records are

637 also a good benchmark for model evaluation. We have especially shown that the isotopic

638 composition of water vapor is a powerful tool to identify aspects to be improved in the general

639 circulation models, such as the horizontal resolution which may influence the representativity

640 of the vertical dynamics.

641

678

Author contributions: AL designed the study and analyzed the data together with FV, CS, EF,
OM. OC installed the water vapor isotopic analyzer in Amsterdam Island and OJ was in charge
of the data calibration. BM and FP performed the measurements of the isotopic composition of
the precipitation samples. CA analyzed the modeling outputs, realized most of the s and
performed model-data analyses. CLDS performed the back trajectory analyses with help from
MC. OM, AD and YB provided expertise on GEM analyses and interpretation. AC, CR, ND
and MW provided model simulations. AL wrote the paper with contribution of all coauthors.

686

Competing interests: One of the coauthors (AD) is a member of the editorial board of
Atmospheric Chemistry and Physics.

689

690

691 **References**

692 Aemisegger, F., Sturm, P., Graf, P., Sodemann, H., Pfahl, S., Knohl, A., and Wernli, H.: Measuring
693 variations of d18O and d2H in atmospheric water vapour using two commercial laser-based
694 spectrometers: an instrument characterisation study, Atmospheric Measurement Techniques, 5, 1491–
695 1511, https://doi.org/10.5194/amt-5-1491-2012, 2012.

696 Aemisegger, F., Spiegel, J., Pfahl, S., Sodemann, H., Eugster, W., and Wernli, H.: Isotope
697 meteorology of cold front passages: A case study combining observations and modeling, Geophysical
698 Research Letters, 42, 5652–5660, 2015.

699 Angot, H., Barret, M., Magand, O., Ramonet, M., and Dommergue, A.: A 2-year record of
700 atmospheric mercury species at a background Southern Hemisphere station on Amsterdam Island,
701 Atmospheric Chemistry and Physics, 14, 11461–11473, 2014.

702 Angot, H., Dion, I, Vogel, N., Legrand, M., Magand, O., and Dommergue, A.: Multi-year record of
703 atmospheric mercury at Dumont d'Urville, East Antarctic coast: continental outflow and oceanic
704 influences, Atmospheric Chemistry and Physics, 16, 8265–8279, 2016.

705 Ansari, M. A., Noble, J., Deodhar, A., and Kumar, U. S.: Atmospheric factors controlling the stable
706 isotopes (δ18O and δ2H) of the Indian summer monsoon precipitation in a drying region of Eastern
707 India, Journal of Hydrology, 584, 124636, 2020.

708 Arias, P., Bellouin, N., Coppola, E., Jones, R., Krinner, G., Marotzke, J., Naik, V., Palmer, M.,
709 Plattner, G.-K., Rogelj, J., and others: Climate Change 2021: the physical science basis. Contribution
710 of Working Group I to the Sixth Assessment Report of the Intergovernmental Panel on Climate
711 Change; technical summary, 2021.

712 Bailey, A., Aemisegger, F., Villiger, L., Los, S. A., Reverdin, G., Quiñones Meléndez, E.,
713 Acquistapace, C., Baranowski, D. B., Böck, T., Bony, S., Bordsdorff, T., Coffman, D., de Szoeke, S.
714 P., Diekmann, C. J., Dütsch, M., Ertl, B., Galewsky, J., Henze, D., Makuch, P., Noone, D., Quinn, P.
715 K., Rösch, M., Schneider, A., Schneider, M., Speich, S., Stevens, B., and Thompson, E. J.: Isotopic
716 measurements in water vapor, precipitation, and seawater during EUREC[4]A, Earth System Science
717 Data, 15, 465–495, https://doi.org/10.5194/essd-15-465-2023, 2023.

718 Benetti, M., Reverdin, G., Pierre, C., Merlivat, L., Risi, C., Steen-larsen, H. C., and Vimeux, F.:
719 Journal of Geophysical Research : Atmospheres during evaporation, 584–593,
720 https://doi.org/10.1002/2013JD020535.Received, 2014.

721 Benetti, M., Aloisi, G., Reverdin, G., Risi, C., and Sèze, G.: Importance of boundary layer mixing for
722 the isotopic composition of surface vapor over the subtropical North Atlantic Ocean, Journal of
723 Geophysical Research: Atmospheres, 120, 2190–2209, 2015.

724 Bhattacharya, S. K., Sarkar, A., and Liang, M.-C.: Vapor isotope probing of typhoons invading the
725 Taiwan region in 2016, Journal of Geophysical Research: Atmospheres, 127, e2022JD036578, 2022.

726 Bloom, N. and Fitzgerald, W. F.: Determination of volatile mercury species at the picogram level by
727 low-temperature gas chromatography with cold-vapour atomic fluorescence detection, Analytica
728 Chimica Acta, 208, 151–161, 1988.

729 Bonne, J. L., Behrens, M., Meyer, H., Kipfstuhl, S., Rabe, B., Schönicke, L., Steen-Larsen, H. C., and
730 Werner, M.: Resolving the controls of water vapour isotopes in the Atlantic sector, Nature
731 Communications, 10, 1–10, https://doi.org/10.1038/s41467-019-09242-6, 2019.

732 Boucher, O., Servonnat, J., Albright, A. L., Aumont, O., Balkanski, Y., Bastrikov, V., Bekki, S.,
733 Bonnet, R., Bony, S., Bopp, L., Braconnot, P., Brockmann, P., Cadule, P., Caubel, A., Cheruy, F.,

734   Codron, F., Cozic, A., Cugnet, D., D'Andrea, F., Davini, P., de Lavergne, C., Denvil, S., Deshayes, J.,
735   Devilliers, M., Ducharne, A., Dufresne, J.-L., Dupont, E., Éthé, C., Fairhead, L., Falletti, L., Flavoni,
736   S., Foujols, M.-A., Gardoll, S., Gastineau, G., Ghattas, J., Grandpeix, J.-Y., Guenet, B., Guez, E.,
737   Lionel, Guilyardi, E., Guimberteau, M., Hauglustaine, D., Hourdin, F., Idelkadi, A., Joussaume, S.,
738   Kageyama, M., Khodri, M., Krinner, G., Lebas, N., Levavasseur, G., Lévy, C., Li, L., Lott, F., Lurton,
739   T., Luyssaert, S., Madec, G., Madeleine, J.-B., Maignan, F., Marchand, M., Marti, O., Mellul, L.,
740   Meurdesoif, Y., Mignot, J., Musat, I., Ottlé, C., Peylin, P., Planton, Y., Polcher, J., Rio, C., Rochetin,
741   N., Rousset, C., Sepulchre, P., Sima, A., Swingedouw, D., Thiéblemont, R., Traore, A. K.,
742   Vancoppenolle, M., Vial, J., Vialard, J., Viovy, N., and Vuichard, N.: Presentation and Evaluation of
743   the IPSL-CM6A-LR Climate Model, Journal of Advances in Modeling Earth Systems, 12,
744   e2019MS002010, https://doi.org/10.1029/2019MS002010, 2020.

745   Bréant, C., Leroy Dos Santos, C., Agosta, C., Casado, M., Fourré, E., Goursaud, S., Masson-Delmotte,
746   V., Favier, V., Cattani, O., Prié, F., Golly, B., Orsi, A., Martinerie, P., and Landais, A.: Coastal water
747   vapor isotopic composition driven by katabatic wind variability in summer at Dumont d'Urville,
748   coastal East Antarctica, Earth and Planetary Science Letters, 514, 37–47,
749   https://doi.org/10.1016/j.epsl.2019.03.004, 2019.

750   Brooks, S.; Ren, X. R.; Cohen, M.; Luke, W. T.; Kelley, P.; Artz, R.; Hynes, A.; Landing, W.; Martos,
751   B. Airborne vertical profiling of mercury speciation near Tullahoma, TN,
752   USA Atmosphere 2014, 5 (3) 557– 574 DOI: 10.3390/atmos5030557.
753
754   Casado, M., Landais, A., Masson-Delmotte, V., Genthon, C., Kerstel, E., Kassi, S., Arnaud, L., Picard,
755   G., Prie, F., Cattani, O., Steen-Larsen, H.-C., Vignon, E., and Cermak, P.: Continuous measurements
756   of isotopic composition of water vapour on the East Antarctic Plateau, Atmospheric Chemistry and
757   Physics, 16, https://doi.org/10.5194/acp-16-8521-2016, 2016.

758   Cauquoin, A. and Werner, M.: High-Resolution Nudged Isotope Modeling With ECHAM6-Wiso:
759   Impacts of Updated Model Physics and ERA5 Reanalysis Data, Journal of Advances in Modeling
760   Earth Systems, 13, e2021MS002532, https://doi.org/10.1029/2021MS002532, 2021.

761   Cauquoin, A., Werner, M., and Lohmann, G.: Water isotopes -- climate relationships for the mid-
762   Holocene and preindustrial period simulated with an isotope-enabled version of MPI-ESM, Climate of
763   the Past, 15, 1913–1937, https://doi.org/10.5194/cp-15-1913-2019, 2019.

764   Craig, H.: Isotopic Variations in Meteoric Waters, Science, 133, 1702–1703,
765   https://doi.org/10.1126/science.133.3465.1702, 1961.

766   Dahinden, F., Aemisegger, F., Wernli, H., Schneider, M., Diekmann, C. J., Ertl, B., Knippertz, P.,
767   Werner, M., and Pfahl, S.: Disentangling different moisture transport pathways over the eastern
768   subtropical North Atlantic using multi-platform isotope observations and high-resolution numerical
769   modelling, Atmospheric Chemistry and Physics, 21, 16319–16347, https://doi.org/10.5194/acp-21-
770   16319-2021, 2021.

771   Dansgaard, W.: Stable isotopes in precipitation., Tellus, 16, 436–468, 1964.

772   Dumarey, R., Temmerman, E., Adams, R., and Hoste, J.: The accuracy of the vapour-injection
773   calibration method for the determination of mercury by amalgamation/cold-vapour atomic absorption
774   spectrometry, Analytica Chimica Acta, 170, 337–340, 1985.

775   Durack, P. J., Taylor, K. E., Ames, S., Po-Chedley, S., and Mauzey, C.: PCMDI AMIP SST and sea-
776   ice boundary conditions version 1.1.8, , https://doi.org/10.22033/ESGF/input4MIPs.16921, 2022.

777   Dütsch, M., Pfahl, S., and Wernli, H.: Drivers of δ2H variations in an idealized extratropical cyclone,
778   Geophysical Research Letters, 43, 5401–5408, 2016.

779 Edwards, B. A., Kushner, D. S., Outridge, P. M., Wang, F. (2021). Fifty years of volcanic mercury
780 emission research: Knowledge gaps and future directions. *Science of The Total Environment*, *757*,
781 143800. https://doi.org/10.1016/j.scitotenv.2020.143800.

783 El Yazidi, A., Ramonet, M., Ciais, P., Broquet, G., Pison, I., Abbaris, A., Brunner, D., Conil, S.,
784 Delmotte, M., Gheusi, F., and others: Identification of spikes associated with local sources in
785 continuous time series of atmospheric CO, CO_2 and CH_4, Atmospheric Measurement Techniques, 11,
786 1599–1614, 2018.

787 Eyring, V., Bony, S., Meehl, G. A., Senior, C. A., Stevens, B., Stouffer, R. J., and Taylor, K. E.:
788 Overview of the Coupled Model Intercomparison Project Phase 6 (CMIP6) experimental design and
789 organization, Geoscientific Model Development, 9, 1937–1958, https://doi.org/10.5194/gmd-9-1937-
790 2016, 2016.

791 Fain, X.; Obrist, D.; Hallar, A. G.; Mccubbin, I.; Rahn, T. High levels of reactive gaseous mercury
792 observed at a high elevation research laboratory in the Rocky Mountains Atmos. Chem.
793 Phys. 2009, 9 (20) 8049– 8060 DOI: 10.5194/acp-9-8049-2009.

795 Fitzgerald, W. F. and Gill, G. A.: Subnanogram determination of mercury by two-stage gold
796 amalgamation and gas phase detection applied to atmospheric analysis, Analytical chemistry, 51,
797 1714–1720, 1979.

798 Fogt, R. and Marshall, G.: The Southern Annular Mode: Variability, trends, and climate impacts
799 across the Southern Hemisphere, Wiley Interdisciplinary Reviews: Climate Change, 11,
800 https://doi.org/10.1002/wcc.652, 2020.

801 Fu, X., Maruszak, N., Wang, X., Gheusi, F. and Sonke, J.: The isotopic composition of gaseous
802 elemental mercury in the free troposphere of the Pic du Midi Observatory, France. Environmental
803 Science & Technology. 50. 10.1021/acs.est.6b00033, 2016

805 Galewsky, J., Steen-Larsen, H. C., Field, R. D., Worden, J., Risi, C., and Schneider, M.: Stable
806 isotopes in atmospheric water vapor and applications to the hydrologic cycle, Reviews of Geophysics,
807 54, 809–865, 2016.

808 Gaudry, A., Ascencio, J., and Lambert, G.: Preliminary study of CO2 variations at Amsterdam Island
809 (Territoire des Terres Australes et Antarctiques Francaises), Journal of Geophysical Research: Oceans,
810 88, 1323–1329, 1983.

811 Graf, P., Wernli, H., Pfahl, S., and Sodemann, H.: A new interpretative framework for below-cloud
812 effects on stable water isotopes in vapour and rain, Atmospheric Chemistry and Physics, 19, 747–765,
813 2019.

814 Gros, V., Poisson, N., Martin, D., Kanakidou, M., and Bonsang, B.: Observations and modeling of the
815 seasonal variation of surface ozone at Amsterdam Island: 1994–1996, Journal of Geophysical
816 Research: Atmospheres, 103, 28103–28109, 1998.

817 Gros, V., Bonsang, B., Martin, D., Novelli, P., and Kazan, V.: Carbon monoxide short term
818 measurements at Amsterdam island: estimations of biomass burning emission rates, Chemosphere-
819 Global Change Science, 1, 163–172, 1999.

820 Gaffney J, Marley N. In-depth review of atmospheric mercury: sources, transformations, and potential
821 sinks. *Energy and Emission Control Technologies*. 2014;2:1-21https://doi.org/10.2147/EECT.S37038.

823 Guilpart, E., Vimeux, F., Evan, S., Brioude, J., Metzger, J., Barthe, C., Risi, C., and Cattani, O.: The
824 isotopic composition of near-surface water vapor at the Maïdo observatory (Reunion Island,

825   southwestern Indian Ocean) documents the controls of the humidity of the subtropical troposphere,
826   Journal of Geophysical Research: Atmospheres, 122, 9628–9650,
827   https://doi.org/10.1002/2017JD026791, 2017.
828
829   Gustin, M. S., Amos, H. M., Huang, J., Miller, M. B., and Heidecorn, K.: Measuring and modeling
830   mercury in the atmosphere: a critical review, Atmos. Chem. Phys., 15, 5697–5713,
831   https://doi.org/10.5194/acp-15-5697-2015, 2015.
832
833   Gustin, M. S., Bank, M. S., Bishop, K., Bowman, K., Brafireun, B., Chételat, J., Eckley, C. S.,
834   Hammerschmidt, C. R., Lamborg, C., Lyman, S., Martínez-Cortizas, A., Sommar, J., Tsz-Ki Tsui, M.,
835   & Zhang, T. (2020). Mercury biogeochemical cycling: A synthesis of recent scientific advances. Science
836   of the Total Environment, 737, 139619. https://doi.org/10.1016/j.scitotenv.2020.139619.
837
838   Gworek, B., Dmuchowski, W. & Baczewska-Dąbrowska, A.H. Mercury in the terrestrial environment:
839   a review. Environ Sci Eur **32**, 128 (2020). https://doi.org/10.1186/s12302-020-00401-x.
840
841   Hersbach, H., Bell, B., Berrisford, P., Hirahara, S., Horányi, A., Muñoz-Sabater, J., Nicolas, J.,
842   Peubey, C., Radu, R., Schepers, D., Simmons, A., Soci, C., Abdalla, S., Abellan, X., Balsamo, G.,
843   Bechtold, P., Biavati, G., Bidlot, J., Bonavita, M., De Chiara, G., Dahlgren, P., Dee, D., Diamantakis,
844   M., Dragani, R., Flemming, J., Forbes, R., Fuentes, M., Geer, A., Haimberger, L., Healy, S., Hogan,
845   R. J., Hólm, E., Janisková, M., Keeley, S., Laloyaux, P., Lopez, P., Lupu, C., Radnoti, G., de Rosnay,
846   P., Rozum, I., Vamborg, F., Villaume, S., and Thépaut, J.-N.: The ERA5 global reanalysis, Quarterly
847   Journal of the Royal Meteorological Society, 146, 1999–2049, https://doi.org/10.1002/qj.3803, 2020.
848   Hoang, C., Magand, O., Brioude, J., Dimuro, A., Brunet, C., Ah-Peng, C., Bertrand, Y., Dommergue,
849   A., Lei, Y. D., and Wania, F.: Probing the limits of sampling gaseous elemental mercury passively in
850   the remote atmosphere, Environ. Sci.: Atmos., 3, 268–281, https://doi.org/10.1039/D2EA00119E,
851   2023.

852   Hourdin, F., Rio, C., Grandpeix, J.-Y., Madeleine, J.-B., Cheruy, F., Rochetin, N., Jam, A., Musat, I.,
853   Idelkadi, A., Fairhead, L., Foujols, M.-A., Mellul, L., Traore, A.-K., Dufresne, J.-L., Boucher, O.,
854   Lefebvre, M.-P., Millour, E., Vignon, E., Jouhaud, J., Diallo, F. B., Lott, F., Gastineau, G., Caubel, A.,
855   Meurdesoif, Y., and Ghattas, J.: LMDZ6A: The Atmospheric Component of the IPSL Climate Model
856   With Improved and Better Tuned Physics, Journal of Advances in Modeling Earth Systems, 12,
857   e2019MS001892, https://doi.org/10.1029/2019MS001892, 2020.

858   Jiskra, M., Sonke, J. E., Obrist, D., Bieser, J., Ebinghaus, R., Myhre, C. L., Pfaffhuber, K. A.,
859   Wängberg, I., Kyllönen, K., Worthy, D., Martin, L. G., Labuschagne, C., Mkololo, T., Ramonet, M.,
860   Magand, O., and Dommergue, A.: A vegetation control on seasonal variations in global atmospheric
861   mercury concentrations, Nature Geoscience, 11, 244–250, https://doi.org/10.1038/s41561-018-0078-8,
862   2018.

863   Koening, A.M., Magand, O., Verreyken, B., Brioude, J., Amelynck, C., Schoon, N., Colomb, A.,
864   Ramonet, M., Sha, M.K., Cammas, J.P., Sonke, J.E., Dommergue, A., 2023. Mercury in the free
865   troposphere and bidirectional atmosphere-vegetation exchanges – Insights from Maido observatory in
866   the southern hemisphere tropics. Atmos. Chem. Phys., 23, 1309-1328, https://doi.org/10.5194/acp-23-
867   1309-2023
868
869   Lee, K.-O., Aemisegger, F., Pfahl, S., Flamant, C., Lacour, J.-L., and Chaboureau, J.-P.: Contrasting
870   stable water isotope signals from convective and large-scale precipitation phases of a heavy
871   precipitation event in southern Italy during HyMeX IOP 13: a modelling perspective, Atmospheric
872   Chemistry and Physics, 19, 7487–7506, 2019.

873   LeGrande, A. N. and Schmidt, G. A.: Global gridded data set of the oxygen isotopic composition in
874   seawater, Geophysical Research Letters, 33, 1–5, https://doi.org/10.1029/2006GL026011, 2006.

875   Leroy-Dos Santos, C., Masson-Delmotte, V., Casado, M., Fourré, E., Steen-Larsen, H. C., Maturilli,
876   M., Orsi, A., Berchet, A., Cattani, O., Minster, B., Gherardi, J., and Landais, A.: A 4.5 Year-Long
877   Record of Svalbard Water Vapor Isotopic Composition Documents Winter Air Mass Origin, Journal
878   of Geophysical Research: Atmospheres, 125, e2020JD032681-e2020JD032681,
879   https://doi.org/10.1029/2020JD032681, 2020.

880   Leroy-Dos Santos, C., Casado, M., Prié, F., Jossoud, O., Kerstel, E., Farradèche, M., Kassi, S., Fourré,
881   E., and Landais, A.: A dedicated robust instrument for water vapor generation at low humidity for use
882   with a laser water isotope analyzer in cold and dry polar regions, Atmospheric Measurement
883   Techniques, 14, 2907–2918, https://doi.org/10.5194/amt-14-2907-2021, 2021.

884   Li, C., Enrico, M., Magand, O., Araujo, B. F., Le Roux, G., Osterwalder, S., Dommergue, A.,
885   Bertrand, Y., Brioude, J., De Vleeschouwer, F., and others: A peat core Hg stable isotope
886   reconstruction of Holocene atmospheric Hg deposition at Amsterdam Island (37.8 oS), Geochimica et
887   Cosmochimica Acta, 341, 62–74, 2023.

888   Lindberg, S., Bullock, R., Ebinghaus, R., Engstrom, D., Feng, X., Fitzgerald, W., Pirrone, N., Prestbo,
889   E., and Seigneur, C.: A synthesis of progress and uncertainties in attributing the sources of mercury in
890   deposition., Ambio, 36, 19–32, 2007, https://doi.org/10.1579/0044-7447(2007)

891   Lyman, S. N.; Jaffe, D. A. Formation and fate of oxidized mercury in the upper troposphere and lower
892   stratosphere Nat. Geosci. 2012, 5 (2) 114–117 doi: 10.1038/ngeo1353
893
894   Magand, O. and Dommergue, A.: Continuous measurements of atmospheric mercury at Maido
895   Observatory (L2), Global Mercury Observation System [data set], 2022.

896   Munksgaard, N. C., Zwart, C., Kurita, N., Bass, A., Nott, J., and Bird, M. I.: Stable isotope anatomy of
897   tropical cyclone Ita, north-eastern Australia, April 2014, PloS one, 10, e0119728, 2015.

898   Murphy, D. M.; Hudson, P. K.; Thomson, D. S.; Sheridan, P. J.; Wilson, J. C. Observations of Mercury-
899   Containing Aerosols. Environ. Sci. Technol. 2006, 40 (10), 3163–3167.
900
901   Noone, D.: Pairing Measurements of the Water Vapor Isotope Ratio with Humidity to Deduce
902   Atmospheric Moistening and Dehydration in the Tropical Midtroposphere, Journal of Climate, 25,
903   4476–4494, https://doi.org/10.1175/JCLI-D-11-00582.1, 2012.

904   Pisso, I., Sollum, E., Grythe, H., Kristiansen, N. I., Cassiani, M., Eckhardt, S., Arnold, D., Morton, D.,
905   Thompson, R. L., Groot Zwaaftink, C. D., Evangeliou, N., Sodemann, H., Haimberger, L, Henne, S.,
906   Brunner, D., Burkhart, J. F., Fouilloux, A., Brioude, J., Philipp, A., Seibert, P., and Stohl, A.: The
907   Lagrangian particle dispersion model FLEXPART version 10.4, Geoscientific Model Development,
908   12, 4955–4997, https://doi.org/10.5194/gmd-12-4955-2019, 2019.

909   Polian, G., Lambert, G., Ardouin, B., and Jegou, A.: Long-range transport of continental radon in
910   subantarctic and antarctic areas, Tellus B: Chemical and Physical Meteorology, 38, 178–189, 1986.

911   Risi, C., Bony, S., Vimeux, F., and Jouzel, J.: Water-stable isotopes in the LMDZ4 general circulation
912   model: Model evaluation for present-day and past climates and applications to climatic interpretations
913   of tropical isotopic records, Journal of Geophysical Research Atmospheres, 115,
914   https://doi.org/10.1029/2009JD013255, 2010.

915   Sciare, J., Mihalopoulos, N., and Dentener, F.: Interannual variability of atmospheric dimethylsulfide
916   in the southern Indian Ocean, Journal of Geophysical Research: Atmospheres, 105, 26369–26377,
917   2000.

918   Sciare, J., Favez, O., Sarda-Estève, R., Oikonomou, K., Cachier, H., and Kazan, V.: Long-term
919   observations of carbonaceous aerosols in the Austral Ocean atmosphere: Evidence of a biogenic
920   marine organic source, Journal of Geophysical Research: Atmospheres, 114, 2009.

921   Shah, V., Jacob, D. J., Thackray, C. P., Wang, X., Sunderland, E. M., Dibble, T. S., Saiz-Lopez, A., Cˇ
922   ernušák, I., Kellö, V., astro, P. J., Wu, R., and Wang, C.: Improved Mechanistic Model of the
923   Atmospheric Redox Chemistry of Mercury, Environ. Sci. Technol., 55, 14445–14456,
924   https://doi.org/10.1021/acs.est.1c03160, 2021.
925
926   Sheu, G. R.; Lin, N. H.; Wang, J. L.; Lee, C. T.; Yang, C. F. O.; Wang, S. H. Temporal distribution and
927   potential sources of atmospheric mercury measured at a high-elevation background station in
928   Taiwan Atmos. Environ. 2010, 44 (20) 2393– 2400 DOI: 10.1016/j.atmosenv.2010.04.009
929
930   Sherwood, S. C., Bony, S., and Dufresne, J.-L.: Spread in model climate sensitivity traced to
931   atmospheric convective mixing, Nature, 505, 37–42, https://doi.org/10.1038/nature12829, 2014.

932   Sillman, S., Marsik, F. J., Al-Wali, K. I., Keeler, G. J., and Landis, M. S.: Reactive mercury in the
933   troposphere: Model formation and results for Florida, the northeastern United States, and the Atlantic
934   Ocean, Journal of Geophysical Research: Atmospheres, 112, 2007.

935   Slemr, F., Angot, H., Dommergue, A., Magand, O., Barret, M., Weigelt, A., Ebinghaus, R., Brunke,
936   E.-G., Pfaffhuber, K. A., Edwards, G., and others: Comparison of mercury concentrations measured at
937   several sites in the Southern Hemisphere, Atmospheric Chemistry and Physics, 15, 3125–3133, 2015.

938   Slemr, F., Martin, L., Labuschagne, C., Mkololo, T., Angot, H., Magand, O., Dommergue, A., Garat,
939   P., Ramonet, M., and Bieser, J.: Atmospheric mercury in the Southern Hemisphere–Part 1: Trend and
940   inter-annual variations in atmospheric mercury at Cape Point, South Africa, in 2007–2017, and on
941   Amsterdam Island in 2012–2017, Atmospheric Chemistry and Physics, 20, 7683–7692, 2020.

942   Sprovieri, F., Pirrone, N., Bencardino, M., D'amore, F., Carbone, F., Cinnirella, S., Mannarino, V.,
943   Landis, M., Ebinghaus, R., Weigelt, A., and others: Atmospheric mercury concentrations observed at
944   ground-based monitoring sites globally distributed in the framework of the GMOS network,
945   Atmospheric chemistry and physics, 16, 11915–11935, 2016.

946   Steen-Larsen, H. C., Johnsen, S. J., Masson-Delmotte, V., Stenni, B., Risi, C., Sodemann, H., Balslev-
947   Clausen, D., Blunier, T., Dahl-Jensen, D., Elleh??j, M. D., Falourd, S., Grindsted, A., Gkinis, V.,
948   Jouzel, J., Popp, T., Sheldon, S., Simonsen, S. B., Sjolte, J., Steffensen, J. P., Sperlich, P.,
949   Sveinbj??rnsd??ttir, A. E., Vinther, B. M., and White, J. W. C.: Continuous monitoring of summer
950   surface water vapor isotopic composition above the Greenland Ice Sheet, Atmospheric Chemistry and
951   Physics, 13, 4815–4828, https://doi.org/10.5194/acp-13-4815-2013, 2013.

952   Steffen, A., Scherz, T., Olson, M., Gay, D., and Blanchard, P.: A comparison of data quality control
953   protocols for atmospheric mercury speciation measurements, Journal of Environmental Monitoring,
954   14, 752–765, 2012.

955   Stevens, B., Giorgetta, M., Esch, M., Mauritsen, T., Crueger, T., Rast, S., Salzmann, M., Schmidt, H.,
956   Bader, J., Block, K., Brokopf, R., Fast, I., Kinne, S., Kornblueh, L., Lohmann, U., Pincus, R.,
957   Reichler, T., and Roeckner, E.: Atmospheric component of the MPI-M Earth System Model:
958   ECHAM6, Journal of Advances in Modeling Earth Systems, 5, 146–172,
959   https://doi.org/10.1002/jame.20015, 2013.

960   Swartzendruber, P., Chand, D., Jaffe, D., Smith, J., Reidmiller, D., Gratz, L., Keeler, J., Strode, S.,
961   Jaeglé, L., and Talbot, R.: Vertical distribution of mercury, CO, ozone, and aerosol scattering
962   coefficient in the Pacific Northwest during the spring 2006 INTEX-B campaign, Journal of
963   Geophysical Research: Atmospheres, 113, 2008.

964   Swartzendruber, P. C., Jaffe, D. A., Prestbo, E., Weiss-Penzias, P., Selin, N. E., Park, R., Jacob, D. J.,
965   Strode, S., and Jaegle, L.: Observations of reactive gaseous mercury in the free troposphere at the
966   Mount Bachelor Observatory, Journal of Geophysical Research: Atmospheres, 111, 2006.

967   Swartzendruber, P.; Chand, D.; Jaffe, D. A.; Smith, J.; Reidmiller, D.; Gratz, L.; Keeler, J.; Strode, S.;
968   Jaegle, L.; Talbot, R. Vertical distribution of mercury, CO, ozone, and aerosol scattering coefficient in
969   the Pacific Northwest during the spring 2006 INTEX-B campaign. J. Geophys. Res., [Atmos.] 2008,
970   113, D10305.
971

972   Talbot, R., Mao, H., Scheuer, E., Dibb, J., and Avery, M.: Total depletion of Hg in the upper
973   troposphere–lower stratosphere, Geophysical Research Letters, 34, 2007.

974   Talbot, R., Mao, H., Scheuer, E., Dibb, J., Avery, M., Browell, E., Sachse, G., Vay, S., Blake, D.,
975   Huey, G., and others: Factors influencing the large-scale distribution of $Hg°$ in the Mexico City area
976   and over the North Pacific, Atmospheric Chemistry and Physics, 8, 2103–2114, 2008.

977   Taylor, K. E., Williamson, D., and Zwiers, F.: The sea surface temperature and sea ice concentration
978   boundary conditions for AMIP II simulations", PCMDI Report 60, Program for Climate Model
979   Diagnosis and Intercomparison,Lawrence Livermore National Laboratory, 2000.

980   Thurnherr, I., Kozachek, A., Graf, P., Weng, Y., Bolshiyanov, D., Landwehr, S., Pfahl, S., Schmale,
981   J., Sodemann, H., Steen-Larsen, H. C., and others: Meridional and vertical variations of the water
982   vapour isotopic composition in the marine boundary layer over the Atlantic and Southern Ocean,
983   Atmospheric Chemistry and Physics, 20, 5811–5835, 2020.

984   Tremoy, G., Vimeux, F., Cattani, O., Mayaki, S., Souley, I., and Favreau, G.: Measurements of water
985   vapor isotope ratios with wavelength-scanned cavity ring-down spectroscopy technology: New
986   insights and important caveats for deuterium excess measurements in tropical areas in comparison
987   with isotope-ratio mass spectrometry, Rapid Communications in Mass Spectrometry, 25, 3469–3480,
988   https://doi.org/10.1002/rcm.5252, 2011.

989   Tremoy, G., Vimeux, F., Mayaki, S., Souley, I., Cattani, O., Risi, C., Favreau, G., and Oi, M.: A 1-
990   year long $\delta 18O$ record of water vapor in Niamey (Niger) reveals insightful atmospheric processes at
991   different timescales, Geophysical Research Letters, 39, 2012.

992   Tremoy, G., Vimeux, F., Soumana, S., Souley, I., Risi, C., Favreau, G., and Oï, M.: Clustering
993   mesoscale convective systems with laser-based water vapor $\delta 18O$ monitoring in Niamey (Niger),
994   Journal of Geophysical Research: Atmospheres, 119, 5079–5103,
995   https://doi.org/10.1002/2013JD020968, 2014.

996   Weiss-Penzias, P.; Gustin, M. S.; Lyman, S. N. Observations of speciated atmospheric mercury at three
997   sites in Nevada: Evidence for a free tropospheric source of reactive gaseous mercury. J. Geophys. Res.
998   [Atmos.] 2009, 114, D14302.
999

1000   Weng, Y., Touzeau, A., and Sodemann, H.: Correcting the impact of the isotope composition on the
1001   mixing ratio dependency of water vapour isotope measurements with cavity ring-down spectrometers,
1002   Atmospheric Measurement Techniques, 13, 3167–3190, https://doi.org/10.5194/amt-13-3167-2020,
1003   2020.

1004   Worden, J., Noone, D., and Bowman, K.: Importance of rain evaporation and continental convection
1005   in the tropical water cycle., Nature, 445, 528–532, https://doi.org/10.1038/nature05508, 2007.

1006